Supporting Information

Gate-Voltage-Modulated Spin Precession in Graphene/WS_2 Field-Effect Transistors

Amir Muhammad Afzal [1,2], Muhammad Farooq Khan [3] and Jonghwa Eom [1,*]

[1] Department of Physics & Astronomy, Graphene Research Institute—Texas Photonics Center International Research Center (GRI–TPC IRC), Sejong University, Seoul 05006, Korea; Amirafzal461@gmail.com
[2] Department of Physics, Riphah International University, 13 Raiwind Road, Lahore 54000, Pakistan
[3] Department of Electrical Engineering, Sejong University, Seoul 05006, Korea; mfk.sejong@gmail.com
* Correspondence: eom@sejong.ac.kr

Device characterization and measurements

Figure S1 shows a schematic diagram showing the fabrication process flow of a graphene/WS_2 field-effect transistor's heterostructure device. First, we cleaned the substrate (SiO_2/p++ Si) with hot acetone and methanol to remove the residue and then dried it with nitrogen. The WS_2 flake was exfoliated on the SiO_2 substrate using Scotch tape, and made a large pattern. Then, we placed the BLG on top of polydimethylsiloxane (PDMS) by mechanical exfoliation from commercial graphite and transferred it onto the WS_2 flake.

Figure S2(a) illustrates an optical microscopy image of the final BLG/ML-WS_2 heterostructure spin FET with ferromagnetic (FM) source and drain contact. Consequently, we made an FM electrode on the BLG/ML-WS_2. The BLG channel length (L) and width (W) were 1 μm and 2.3 μm, respectively. To observe the surface morphology of WS_2 and BLG, AFM was used. AFM was used to confirm the thickness of ML-WS_2 and BLG on SiO_2 (Fig. S2(b)). The height profiles reveal the thickness of ML-WS_2 (~19 nm) and BLG (~0.8 nm) in Fig. S2(c) and (d), respectively.

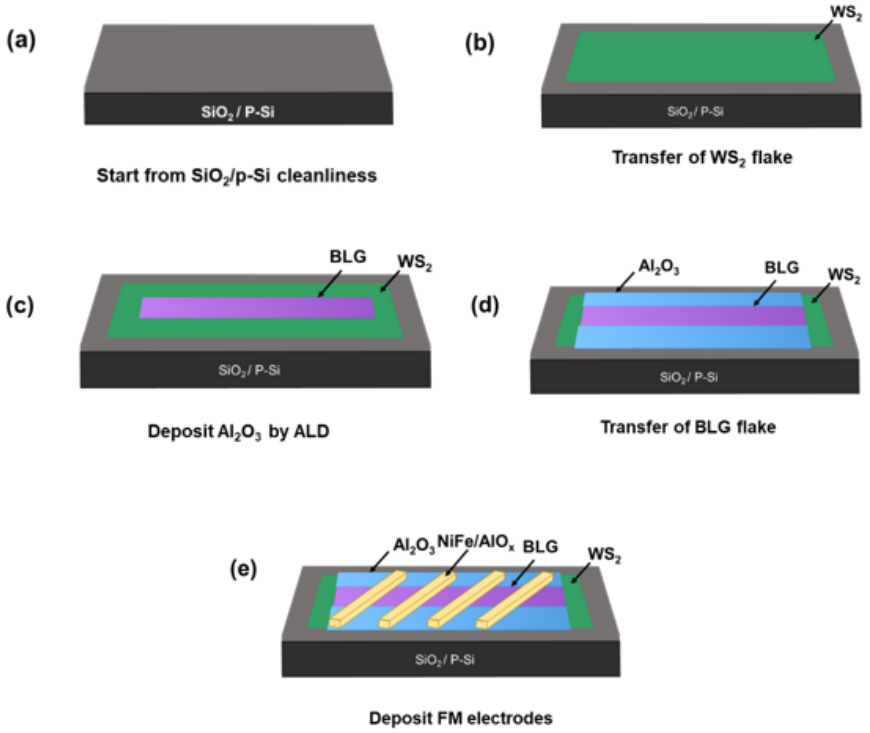

Figure S1. Schematic diagram showing the fabrication process flow of a graphene/WS2 field-effect transistor's heterostructure device. (a)–(e) Schematic procedures of the device fabrication.

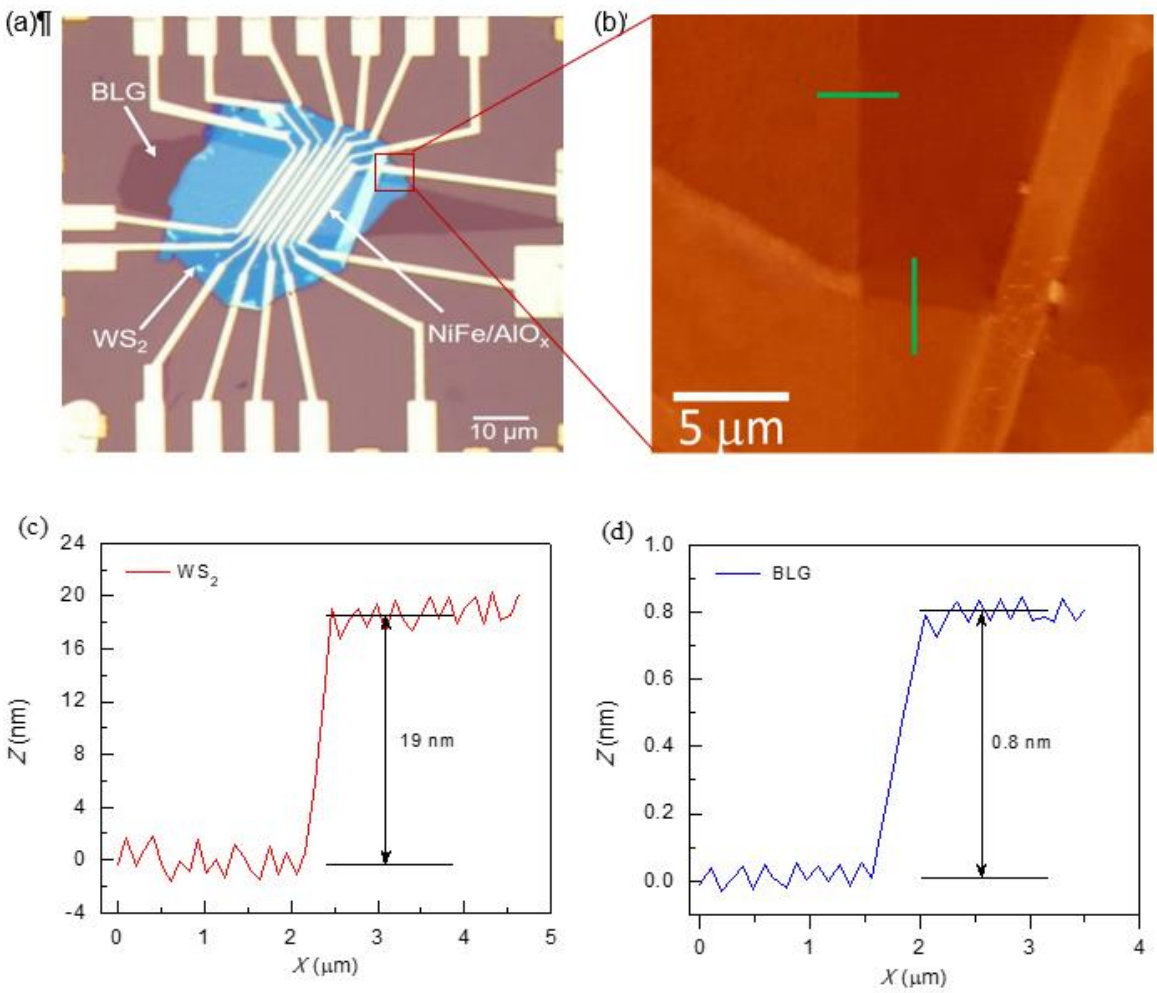

Figure S2. Structure of the BLG/ML-WS_2 spin FET. (a) An optical microscope image of the BLG/ML-WS_2 heterostructure device with FM source and drain contact with local measurement geometry. The FM electrodes are patterned at 45° with respect to the BLG channel. The length and width of the graphene channel were 1 μm and 2.3 μm, respectively. (b) AFM image of the device showing WS_2 and BLG on SiO_2. (c) The height profile of WS_2. The thickness of the WS_2 is ~19 nm. (d) The height profile of BLG. The thickness of the BLG flake is ~0.8 nm.

Raman spectra of the BLG/ML-WS_2 spin FET

To identify the structural fingerprint of both BLG and WS_2, the Raman spectra were examined with a Renishaw micro-spectrometer over a wavenumber range of 1100 to 3200 cm^{-1} for BLG and 200 to 500 cm^{-1} for WS_2 with a laser of 514.5 nm. To avoid local heating, the power was fixed to less than ~1.0 mW with a spot size of 1 μm. The Raman spectra of ML-WS_2 and BLG on SiO_2 are shown in Fig. S3(a) and (b). The E_{2g}^1 and A_1 peaks of WS_2 appear at 351 cm^{-1} and 418 cm^{-1}, respectively.

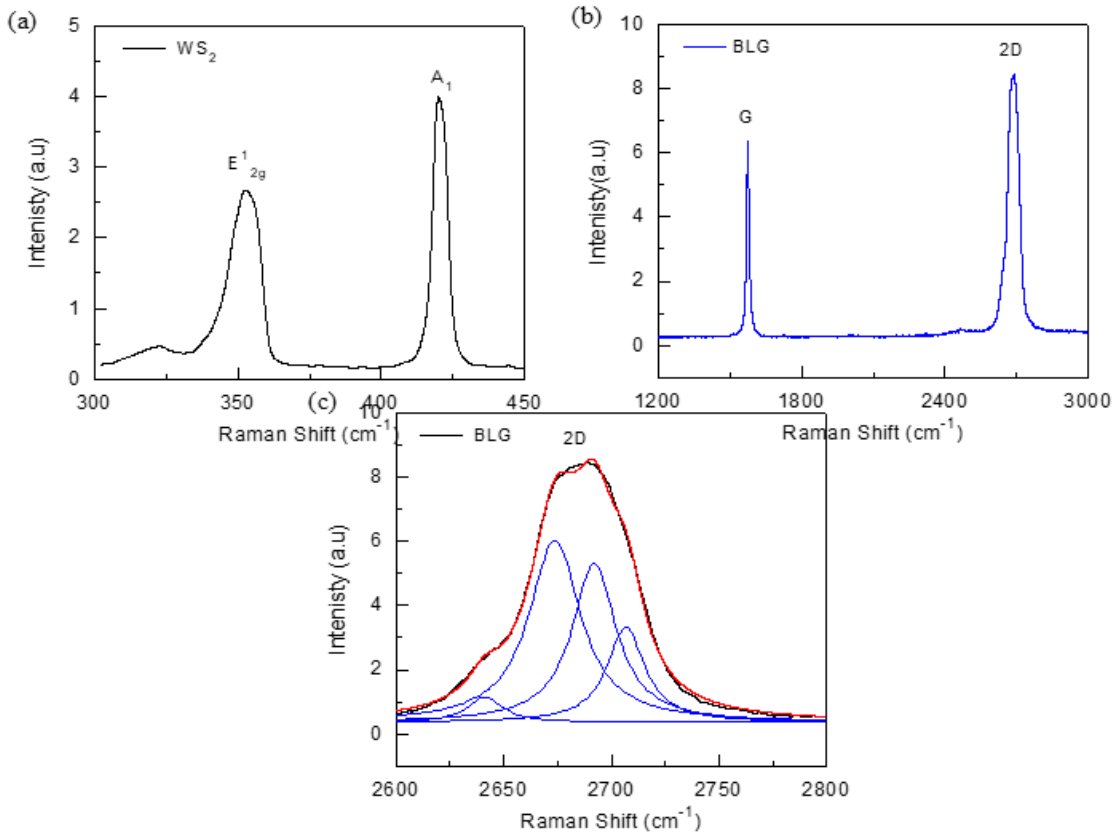

Figure S3. Raman spectra of the BLG/ML-WS_2 spin FET. (a) Raman spectrum of multilayers of WS_2. The peaks E^1_{2g} and A_1 appear at 351 cm^{-1} and 418 cm^{-1}, respectively. (b) Raman spectrum of BLG. (c) Raman spectrum of BLG 2D peak. The peak is fitted by four Lorentzian peaks, which confirm the nature of BLG.

In the case of BLG, the Raman G and 2D peaks appear around 1587 cm^{-1} and 2685 cm^{-1}, respectively. The ratio of intensities of the G to 2D peaks (I_{2D}/I_G) is ~1.2, which is consistent with the previously reported value for BLG [1]. Further, the 2D peak is fitted by four Lorentzian peaks, which confirm the nature of BLG (Fig. S3(c)).

Dirac Point measurement of BLG on WS_2

First, we characterized the basic electrical transport properties of Gr/WS_2 vdW heterostructure devices (sample # 2) to confirm the disappearance of the Dirac point in the case of an FM electrode. Fig. S4(a) shows the final device, in which graphene is outlined by the white dashed line. The different pairs of FM and Cr/Au electrodes were patterned by electron-beam lithography on WS_2, BLG, and BLG/WS_2 heterostructure devices (Fig. S4(a)). First, we measured the transfer characteristics as a function of V_{bg} of WS_2 with Cr/Au (purple circle) and determined the threshold voltage (V_{th}~ 10 V), as shown in Fig. S4(b).

Secondly, we made NiFe (red circle) and Cr/Au (blue circle) electrodes on BLG/SiO_2 and measured their electrical transport properties (Fig. S4(a)). The resistance (R_{xx}) of BLG as a function of back-gate voltage (V_{bg}) is shown in Fig. S4(c). V_{bg} is swept from -40 V to +40 V, and resistance is measured. In the case of Cr/Au, the charge neutrality point (CNT) (i.e., the Dirac point) almost exits at V_{bg}~ 2 V. However, in the case of the NiFe electrode, the CNT is shifted at V_{bg}~ 31 V due to p-type doping of graphene by NiFe, as shown in Fig. S4(c).

Thirdly, we measured the BLG/WS_2 heterostructure with Cr/Au and NiFe contacts. We observed that the CNT lies at V_{bg}~ 0 V for Cr/Au electrodes. When V_{bg} is increased from -40 V, the resistance of the Gr/WS_2 heterostructure device increases until V_{bg} reaches the CNT. However, the resistance is asymmetric with respect to the CNT. The resistance of the heterostructure device does not change when V_{bg} is increased above the threshold voltage (V_{th} ~ 10 V) of the bottom WS_2 layer. However, we measured the BLG/WS_2 heterostructure with NiFe electrodes and did not

observe any Dirac point, as shown in Fig. S4(c). In fact, the NiFe electrode shifts the Daric point at positive back-gate voltage (V_{bg}~ 31 V) by p-type doping, and the bottom WS_2 layer works in a similar manner to a gate electric field sink at $V_{bg} > V_{th}$ ~ 10 V. At $V_{bg} > 10$ V (gate voltages larger than the threshold voltage of WS_2), the electrons start to accumulate at the bottom surface of the WS_2 flake and screen the influence of the gate electric field.

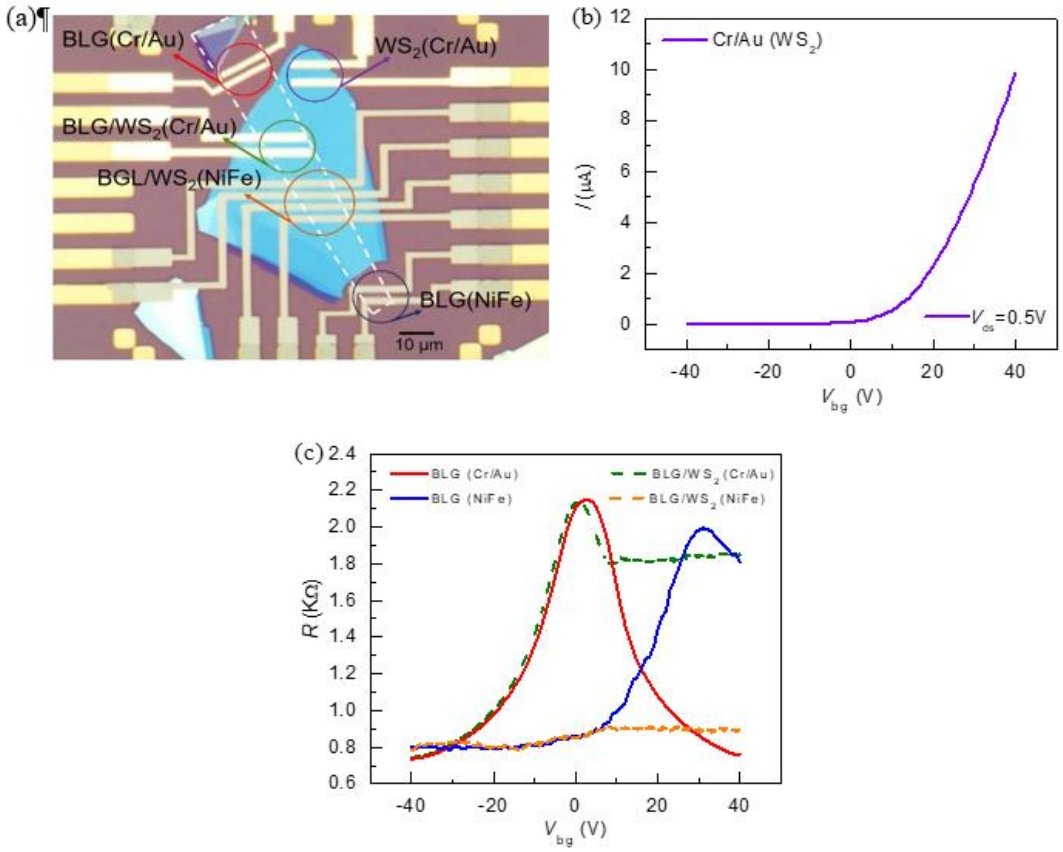

Figure S4. Doping effect by NiFe electrodes and screening effect by WS_2 layer. (a) An optical image of the final device in which graphene is marked with the white dashed line on SiO_2 and WS_2 (sample #2). The different pairs of NiFe and Cr/Au electrodes were patterned by electron-beam lithography on WS_2, BLG, and BLG/WS_2 heterostructure devices, which are illustrated by purple, red, green, orange, and blue circles for WS_2 (Cr/Au), BLG (Cr/Au), BLG/WS_2 (Cr/Au), BLG/WS_2 (NiFe), and BLG (NiFe), respectively. (b) The transfer characteristics as a function of V_{bg} of WS_2 with Cr/Au (purple circle); the threshold voltage (V_{th}) was found around 10 V. (c) The resistance of BLG on SiO_2 and WS_2 as a function of back-gate voltage (V_{bg}) with different electrodes.

Gate-dependent Hanle spin precession measurement

We performed experiments on NL Hanle spin precession signals at various V_{bg}. For this purpose, we applied an in-plane magnetic field, $B_{\parallel}$, to align the magnetization of FM contacts parallel or antiparallel to each other. The perpendicular magnetic field ($B_{\perp}$) was then swept to detect the Hanle spin signal. Fig. S5(a) shows the gate-dependent NL Hanle spin signal at different back-gate voltages. Each trace was taken with 10 V steps in the back gate from $V_{bg} = -40\,V$ to $+40\,V$. Then, we calculated the change in NL Hanle spin signal ($\Delta R_{NL} = R_{NL}^{Parallel} - R_{NL}^{Anti-parallel}/2$) at all V_{bg}.

By fitting the raw data of the Hanle spin signal (ΔR_{NL}) using Equation (3), we extracted τ_s in the range of $\tau_s \approx 66.05 - 2.02\,ps$, depending on V_{bg}. Furthermore, we calculated the Rashba-type SOI strength ($\circledcirc \approx 6.14$ meVnm) using Equation (4). Fig. S5(b) indicates the α of the spin FET as a function of V_{bg}. For $V_{bg} < 0$, V_{bg} efficiently changes α, whereas α does not change much when $V_{bg} > 0$ due to the screening effect of the n-type WS_2 film. From the Rashba parameter α, we obtained the spin precession angle with respect to V_{bg} by using Equation (5), as shown in Fig. S5(c). When V_{bg} was varied from -40 to +40 V in our BLG/ML-WS_2 spin FET, the total change of precession angle was $\Delta\theta \approx 319^{\circ}$.

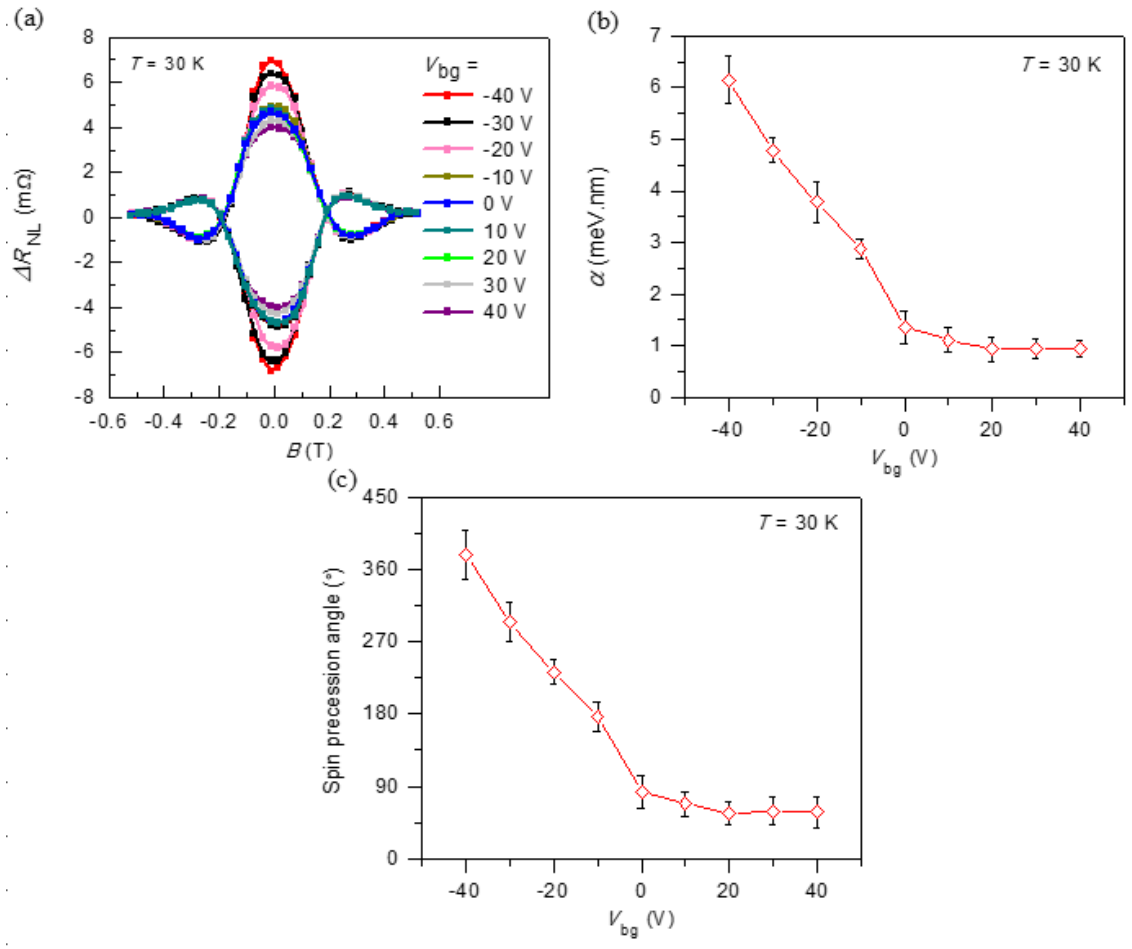

Figure S5. Gate modulation of spin precession angle in the BLG/ML-WS_2 spin FET. (a) Modulation of Hanle spin precession with back-gate voltage. Hanle spin signal measured at different back gates at 30 K. (b) Gate voltage dependence of the spin–orbit interaction parameter ⍟. (c) Estimated spin precession angle as a function of V_{bg} at 30 K.

Spin transport parameters

By fitting the raw data of the Hanle spin signal ($\Delta R_{NL} = R_{NL}^{Parallel} - R_{NL}^{Anti-parallel}/2$) at all V_{bg} using Equation (3), we extracted τ_s in the range of $\tau_s \approx 66.05 - 2.02\ ps$ depending on V_{bg}, as shown in Fig. S6(a). Further, we calculated momentum scattering time, τ_P, from $D = v_F^2 \tau_P$, where v_F is the Fermi velocity and D is a diffusion constant calculated using the Einstein relation $\sigma = e^2 D\, N_{2D}(E_F)$, where $N_{2D}(E_F)$ is the density of states of graphene at the Fermi level.

We determined that both quantities were inversely proportional to each other, and the D'yakonov–Perel' (DP) mechanism is dominant. We observed a clear relation at V_{bg} = -40 V to 10V. However, at a higher back-gate voltage (V_{bg} > 10 V), we did not perceive a large change in either quantity due to the WS_2 contribution. Fig. S6(b) demonstrates the spin diffusion length ($\lambda_s = \sqrt{D_s \tau_s}$) as being in the range of $0.98 - 0.15\ \mu m$ depending on V_{bg}. By using the values of τ_P and τ_s from Fig. S6(a), we calculated the Rashba spin splitting (Δ_R) using $\frac{1}{\tau_s} = \frac{4\Delta_R^2}{\hbar^2}\tau_P$, as shown in Fig. S6(c).

We have compared physical quantities of our bilayer graphene/multilayer WS_2 field-effect transistor with previously reported parameters of graphene in Table S1.

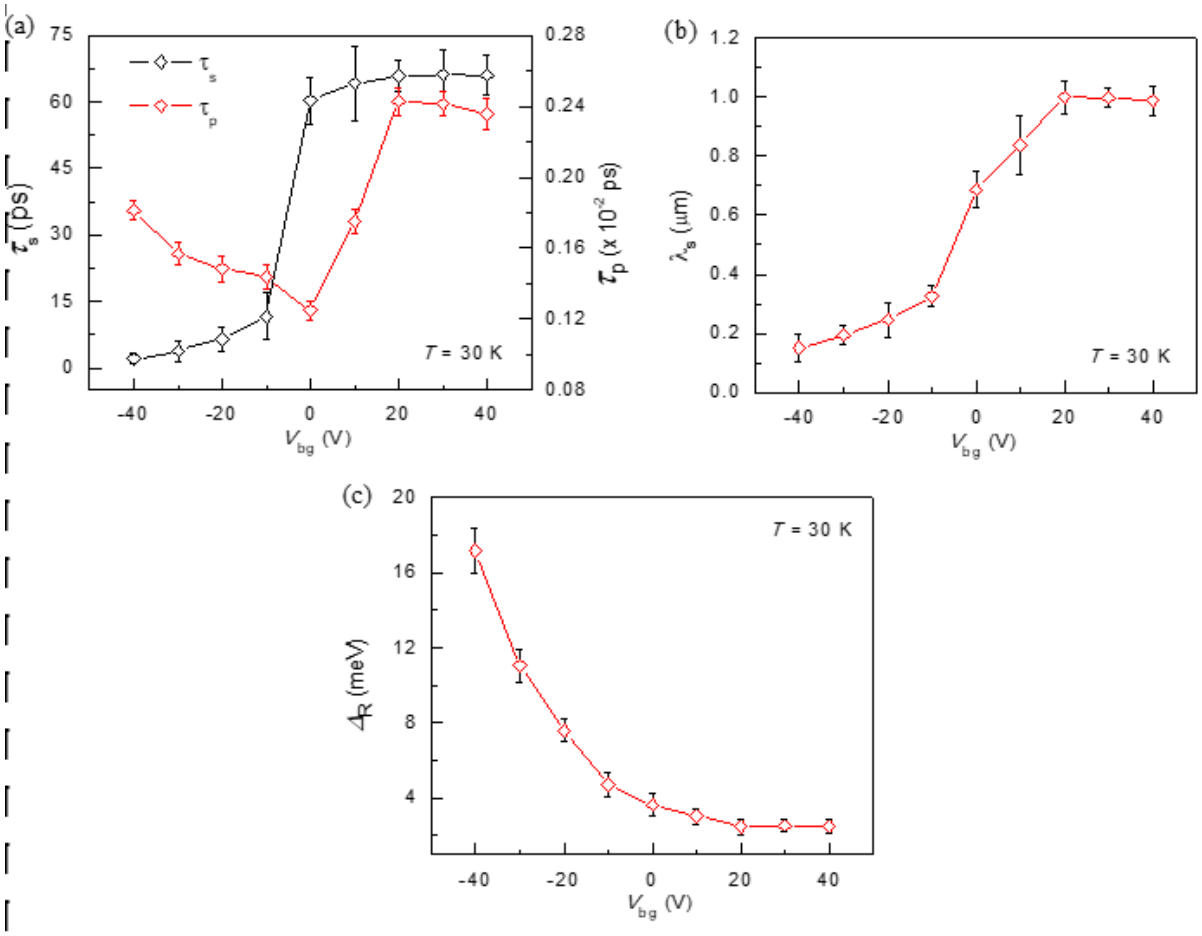

Figure S6. Spin transport parameters. **(**a) Gate dependence of τ_s, which is derived from the fitting of the Hanle spin precession in Equation (3). (b) Gate dependence of λ_s. (c) Rashba spin splitting (Δ_R) as a function of V_{bg} at 30 K.

Table S1. Comparison of key parameters of bilayer graphene/multilayer WS_2 field-effect transistor with previously reported parameters in pristine graphene.

Devices	**λ_s (μm)**	**τ_s (ps)**	**α (meVnm)**	**$\Delta\theta$ (°)**	**Ref.**
Gr	0.8	172	------	------	[2]
Gr/h-BN	0.7	105	------	------	[3]
Gr	0.65	100	------	------	[4]
Gr	1.4	84	------	------	[5]
Gr	1.3	125	------	------	[6]
Gr/WS_2	0.98	2.02	6	309	This work

.

References

1. Ferrari, A.C.; Meyer, J.C.; Scardaci, V.; Casiraghi, C.; Lazzeri, M.; Mauri, F.; Piscanec, S.; Jiang, D.; Novoselov, K.S.; Roth, S.J.P.r.l. Raman spectrum of graphene and graphene layers. **2006**, *97*, 187401.
2. Dankert, A.; Kamalakar, M.V.; Bergsten, J.; Dash, S.P.J.A.P.L. Spin transport and precession in graphene measured by nonlocal and three-terminal methods. **2014**, *104*, 192403.
3. Kamalakar, M.V.; Dankert, A.; Kelly, P.J.; Dash, S.P.J.S.r. Inversion of spin signal and spin filtering in ferromagnet| hexagonal boron nitride-graphene van der Waals heterostructures. **2016**, *6*, 1-9.
4. Jedema, F.; Heersche, H.; Filip, A.; Baselmans, J.; Van Wees, B.J.N. Electrical detection of spin precession in a metallic mesoscopic spin valve. **2002**, *416*, 713-716.
5. Han, W.; Pi, K.; Bao, W.; McCreary, K.; Li, Y.; Wang, W.; Lau, C.; Kawakami, R.J.A.P.L. Electrical detection of spin precession in single layer graphene spin valves with transparent contacts. **2009**, *94*, 222109.
6. Tombros, N.; Jozsa, C.; Popinciuc, M.; Jonkman, H.T.; Van Wees, B.J.J.n. Electronic spin transport and spin precession in single graphene layers at room temperature. **2007**, *448*, 571-574.